Zeitschrift für Physikalische Chemie, **215**, 10, 1323–1339 (2001)

The Spectral Momentum Density of Aluminium, Copper and Gold Measured by Electron Momentum Spectroscopy

By A. S. Kheifets*, M. Vos and E. Weigold

Atomic and Molecular Physics Laboratories, Research School of Physical Sciences and Engineering, Institute of Advanced Studies, Australian National University, Canberra, ACT 0200, Australia

Dedicated to Prof. Dr. Dr. h.c. Wolf Weyrich on the occasion of his 60th birthday

(Received July 11, 2001; accepted July 16, 2001)

Electronic Structure / Metals / Electron Momentum Spectroscopy

Electron momentum spectroscopy (EMS) gives direct information of the full energy-resolved electron momentum densities of occupied states (bands) in solids – single crystal, polycrystalline or amorphous. Here we present data from a new high energy EMS spectrometer using 50 keV incident and 25 keV outgoing electrons, on polycrystalline specimens of aluminium, copper and gold. The spectral momentum densities show very significant electron-electron correlation effects which are in good agreement with many-body Green's function calculations.

1. Introduction

The measurement of the full spectral electron momentum density (SEMD) of solids is of great interest since it can be compared directly with calculations of the ground state electronic structure of the solid. Different experimental techniques have been developed to look at different aspects of the spectral momentum density. Thus angle-resolved photo-electron spectroscopy [1] (ARPES) is very successful in providing high resolution measurements of the energy dispersion of occupied states in single crystals. Information on the electron momentum density (EMD), which is directly related to the wavefunction, has generally been obtained through positron annihilation experiments (ACAR) [2] or by Compton scattering using either photons [3, 4] or electrons [5] as projectiles. Both of these techniques give no information on the energy dependence

* E-mail: a.kheifets@anu.edu.au

of the spectral momentum densities. Strictly speaking ACAR does not measure EMD's but the electron-positron pair density, i.e. the EMD weighted by the positron wavefunction. In a perfect crystal annihilation spectroscopy samples the least bound electrons preferentially, and hence its main use is to map Fermi surfaces in metals. Since the positron is repelled by the nuclei, ACAR also provides a sensitive probe of defect sites in solids. On the other hand, the Compton profile, obtained by high-energy high-momentum-transfer electron or photon collisions, is the projection of the momentum density on the direction of momentum transfer integrated over the binding energies of the struck electrons.

If the recoil electron is measured in coincidence with the scattered photon [6, 7] or electron [8, 9], and the full collision kinematics is determined in respectively (γ, eγ) and (e, 2e) measurements, it allows the complete reconstruction of the initial electron binding energy and momentum, yielding the 3D-SEMD in contrast to the 1D-EMD information of the Compton profile.

As the electron-electron scattering cross section (Mott) is orders of magnitude larger than the photon-electron scattering cross section (Klein-Nishina), (e, 2e) experiments can be made with much better resolution than (γ, eγ) investigations. Indeed (γ, eγ) measurements have to date been unable to resolve energy information in the valence region, whereas the (e, 2e) technique, or electron momentum spectroscopy (EMS), has been successful in measuring the energy dispersion of bands as well as their electron momentum density distribution with around 1 eV energy resolution and momentum resolution of 0.1 a.u. [9]. The energy dispersion information obtained by EMS resembles ARPES (with at present poorer energy resolution), though EMS is not limited to crystals and its interpretation is more straight forward [9].

A major problem for (e, 2e), and to a lesser extent for (γ, eγ), is the strong cross section for incoherent electron scattering in solids. The mean free path for elastic and inelastic scattering of electrons in the 10 keV range is only a few 10 nm, hence the target specimens need to be very thin self-supporting foils. In EMS measurements the diameters of the foils need to be only of the order of 100 μm, whereas in (γ, eγ) they need to be much larger due to lower γ fluxes and (γ, eγ) cross sections. The other effect of multiple scattering is to remove (e, 2e) events from the true SEMD distribution to other parts of the energy-momentum phase-space. Elastic scattering changes the inferred momentum of the original (e, 2e) event from its true value, thus leading to a smeared-out background underlying the real SEMD events. Inelastic scattering, mainly due to plasmon excitation, leads to events with increased binding energies. Ways of correcting for these unwanted multiple scattering effects are discussed in Section 3.

The rest of the paper is set out as follows. Section 2 gives the theoretical background to EMS measurements. The experimental apparatus and technique

are outlined in Section 3 and the theoretical methods used to calculate SEMD's in Section 4. Some experimental and theoretical results for the metals aluminium, copper and gold are discussed in Section 5.

2. Theoretical background to EMS

At high electron energies and for high momentum transfer collisions, the binary encounter approximation is valid and the collision can be treated as an electron-electron collision with the rest of the (recoiling) ionised system essentially being a spectator. Exchange between the bound and free electrons can also be neglected because the overlap of the wavefunctions of the high momentum free electrons with the relatively low momentum bound electrons is vanishingly small. At high enough energies the continuum electrons can be treated as plane waves, and the plane wave impulse approximation (PWIA) is valid.

The momentum $\boldsymbol{q}$ of the struck electron can be inferred from momentum conservation

$$\boldsymbol{q} = \boldsymbol{k}_1 + \boldsymbol{k}_2 - \boldsymbol{k}_0 \,, \tag{1}$$

where the subscripts 0, 1, 2 refer respectively to the incident and two outgoing electrons, the faster of which is normally referred to as the scattered electron. The separation or binding energy of the ejected electron is given by

$$\varepsilon = E_0 - E_1 - E_2 \,. \tag{2}$$

In the PWIA the (e, 2e) differential cross section is given, in atomic units with $e = m_e = \hbar = 1$, by the following expression:

$$\sigma(\boldsymbol{k}_0, \boldsymbol{k}_1, \boldsymbol{k}_2; \varepsilon) = (2\pi)^4 \frac{k_1 k_2}{k_0} \frac{N}{4\pi} f_{ee}\, \rho(\boldsymbol{q}, \varepsilon) \quad , \tag{3}$$

where the the full spectral electron momentum density (SEMD) is

$$\rho(\boldsymbol{q}, \varepsilon) = \sum_i |\langle \boldsymbol{q} | \psi_i \rangle|^2 \, \pi^{-1} \, \mathrm{Im}\, G_i^-(\varepsilon) \,. \tag{4}$$

In writing this expression we presume that the single-hole Green's function of the many-electron target $G_i^-(\varepsilon)$ can be diagonalised on an appropriate basis of quasi-particle states (electron shells in atoms, Bloch waves in crystals etc.), and we take the Fourier transform of the one-electron orbital ψ_i. The collision factor f_{ee} is the half-off-shell Mott electron-electron scattering cross section. This factor is constant for the non-coplanar symmetric kinematics when $E_1 = E_2$, the incident direction being the $z-$axis with $\theta_1 = \theta_2 =$ constant and $\phi = \pi - \phi_1 - \phi_2$ is varied.

The imaginary part of the single-hole Green's function is calculated as

$$\text{Im } G_i^-(\varepsilon) = \sum_\alpha |\ \langle N-1, \alpha \mid \hat{a}_i \mid N, 0\rangle\ |^2\ \delta(\varepsilon - E_{N-1,\alpha} + E_{N,0})\,, \tag{5}$$

where $\hat{a}_i$ is the annihilation operator which removes an electron defined by the quantum label i from the ground state of the system of N interacting electrons $|N, 0\rangle$. This sudden removal creates a state which is a superposition of the eigenstates of the ionised system $|N-1, \alpha\rangle$. Only those states contribute which are compatible with the energy conservation. For an extended system (a crystal) the momentum conservation has also to be satisfied and Eq. (4) takes the form:

$$\rho(\boldsymbol{q}, \varepsilon) = \sum_{j,\boldsymbol{k},\boldsymbol{G}} |\langle \boldsymbol{q}|\psi_{j\boldsymbol{k}}\rangle|^2\ \delta_{\boldsymbol{q},\boldsymbol{k}+\boldsymbol{G}}\ \ \pi^{-1}\ \text{Im } G_j^-(\boldsymbol{k}, \varepsilon) \tag{6}$$

Here j is the band index, $\boldsymbol{k}$ is the crystalline momentum and $\boldsymbol{G}$ is the reciprocal lattice vector.

In the absence of electron-electron interaction $\pi^{-1}\text{Im } G_j^-(\boldsymbol{k}, \varepsilon) = \delta(\varepsilon - \varepsilon_{j\boldsymbol{k}})$ and the spectrum contains only one delta-function line following the band dispersion. The interacting SEMD (6) contains much more information than a simple band dispersion. The main spectral feature associated with $\text{Im } G_j^-(\boldsymbol{k}, \varepsilon)$ describes the quasi-particle in the band j having momentum $\boldsymbol{k}$ and energy ε. The centre of the quasi-particle peak is shifted with respect to the one-electron energy $\varepsilon_{j\boldsymbol{k}}$. The peak acquires a final width due to the quasi-particle lifetime. In addition, a satellite structure arises from electron-electron correlations. This can all be measured in EMS.

It is important to note that the momenta $\boldsymbol{q}$ measured in EMS are real momenta and not crystal momenta $\boldsymbol{k}$. Thus EMS works equally well for polycrystalline and amorphous materials as well as single crystal specimens. However, except for single crystal specimens, there is in general, no preferred direction in space and the cross section measures a spherically averaged $\rho(q,\ \varepsilon)$.

3. Experimental technique

In the new high energy EMS apparatus at the Australian National University [10] both detectors for the outgoing electrons are placed at symmetric polar angles relative to the incident electron ($\theta_1 = \theta_2 = \theta_s = 44.3^\circ$) and select electrons of equal mean energies $E_1 = E_2 = 25$ keV. The incident energy is 50 keV plus an offset to allow for the binding energies. In this arrangement coplanar events have $q = 0$. The detected electrons pass through two identical hemispherical analysers before impinging on a position sensitive detector (PSD) comprised of channel plates and a resistive anode. The analysers accept electrons over a range of azimuthal angles, $|\ \phi_1\ | \leq 5^\circ$ and $|\ \phi_2\ | \leq 5^\circ$, where ϕ_1 and

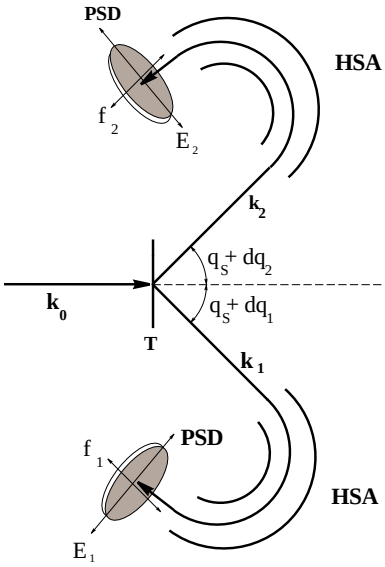

Fig. 1. Schematic of the EMS apparatus. The incident beam of energy E_0 and momentum $\boldsymbol{k}_0$ is incident on a thin foil target T. The scattered and ejected electrons emerge at polar angles $\theta_s + \delta\theta_i$ and equal mean energies $\overline{E}_1 = \overline{E}_2$. After retardation and traversal through hemispherical electrostatic analysers (HSA) they are analysed in energy and out of horizontal plane azimuthal angles ϕ_i by position sensitive electron detectors (PSD).

ϕ_2 are the azimuthal angles of the detected electrons relative to the median scattering plane which is the horizontal plane. After deceleration the mean electron pass energy in the analysers is set either at 250 eV corresponding to an energy window $\Delta E_1 = \Delta E_2 = 50$ eV, or 400 eV with $\Delta E_1 = \Delta E_2 = 80$ eV. The two dimensional detectors allow both the energy and angles to be determined for each electron. The experimental setup is sketched in Fig. 1. It and the characteristics of the apparatus are described fully in Vos *et al.* [10] and Vos and Weigold [11] and need not be repeated here.

The coordinate system can be defined by choosing the $z-$direction parallel to $\boldsymbol{k}_0$ and the $x-$direction being in the mean scattering (horizontal) plane. The $y-$direction is then the vertical direction. The polar angles θ_1 and θ_2 can be changed from the normal values of 44.3° (smaller than 45° due to relativistic corrections for scattering from a stationary electron) by $\delta\theta_1$ and $\delta\theta_2$ by applying suitable voltages on pairs of deflectors placed between the specimen and the essentially vertical slits with $\theta = \theta_s$ situated before the decelerating lenses of the analysers. For normal operation with $\delta\theta_1 = \delta\theta_2 = 0$ and $k_1 = k_2$ one obtains

$$q_y = q_1(\phi_1 + \phi_2) \tag{7}$$

$$q_x = q_z = 0 \tag{8}$$

Here we have ignored the possible small differences in k_1 and k_2 due to the finite energy acceptance window. This can lead to a small finite k_z component. However $k_1 - k_2 \leq 0.04$ a.u. for 25 keV electrons ($k_1 = 43.3$ a.u. and $\Delta E = 50$ eV). With the deflectors in operation one obtains non-zero offsets for q_x and q_z so that the range of momenta swept out by q_y no longer goes through the Γ point with $\boldsymbol{q} = 0$. The offsets are given by

$$q_x = k_1 \cos\theta_s(\delta\theta_2 - \delta\theta_1), \tag{9}$$

$$q_z = k_1 \sin\theta_s(\delta\theta_1 + \delta\theta_2) \tag{10}$$

This allows one to make different cuts through the Brillouin zone for fixed values of q_x and q_z. For $\delta\theta_1 = \delta\theta_2$ the cuts are with $q_z \neq 0$ and $q_x = 0$, whereas for $\delta\theta_1 = -\delta\theta_2$ the cuts are for $q_x \neq 0$ and $q_z = 0$. Currently the incident beam is not monochromatised and the overall long term binding energy resolution is around 1.5 eV, whereas the momentum resolution $\Delta q_y \lesssim 0.1$ a.u.

Even at incident energies of 50 keV and emitted electron energies of 25 keV and with thin ($\sim 5-3$ nm) foil target specimens, multiple scattering by the electrons in traversing the target must be corrected for. Inelastic collisions, mainly due to plasmon creation by the incoming and outgoing electrons before and after the (e, 2e) event, shift the detected (e, 2e) event to a higher binding energy. Momentum changes associated with plasmon creation are small and therefore do not significantly affect the inferred momentum densities.

Since the plasmon energy spread can be quite broad and more than one plasmon can contribute, this can lead to a tail (with peaks) in the energy dimension of the measured intensity, reflecting density shifted in energy and broadened by the widths of the plasmons. This can be corrected for by measuring in-situ the elastic and energy loss spectrum. Elastic scattering on the other hand does not change the binding energy ε but does change the observed momentum from its true value $\boldsymbol{q}$ by

$$\Delta\boldsymbol{q} = \boldsymbol{q}_{\text{obs}} - \boldsymbol{q} = \Delta\boldsymbol{k}_0 - \Delta\boldsymbol{k}_1 - \Delta\boldsymbol{k}_2 \tag{11}$$

with $\Delta\mathbf{k}_i$ the change of momentum caused by elastic scattering of the incident and/or emitted electrons. Since $\boldsymbol{q}_{\text{obs}}$ is always directed along the $y-$axis, it is clear that electrons with $\boldsymbol{q}$ directed away from the $y-$axis can contribute to the observed events. Thus target electrons with different momenta and energy ε can contribute to the intensity at $\boldsymbol{q}_{\text{obs}}(\varepsilon)$ [12]. At high energies the partial wave expansion method provides a good description of the elastic cross sections and can be used to evaluate the spread $\Delta\boldsymbol{q}$ of events due to multiple scattering. Vos and Bottema [12] have developed a Monte-Carlo technique to convolute theoretical spectral momentum densities for the effects of both elastic and inelastic multiple scattering, and thus allow for a direct comparison of theory with the measurements. Although deconvolution of the data for inelastic multiple scattering is relatively straightforward as discussed above, that of elastic scattering

is not. It is therefore necessary to use high energies and thin targets to minimise these effects.

The preparation of typical target membranes of diameter 0.1–0.3 mm and thickness 5–20 nm is described by Fang *et al.* [13]. Samples are first thinned by cleaving and/or chemical or electrochemical etching. Films can also be simply prepared on a surface which dissolves in solution (e.g. a surfactant or single crystal of salt in water), and the floating films can then be lifted off the surface of the solvent by a suitable mount. These samples can be further thinned and cleaned by reactive plasma etching or ion bombardment. This is done in a UHV preparation chamber separate from the main spectrometer. Annealing and specimen characterisation with an Auger system can be carried out in an intermediate buffer chamber. Targets can also be prepared in this chamber by evaporation onto a surface of a thin membrane (usually carbon). Argon ion etching can be done in this chamber, to thin and clean the surface of the specimen or to thin or remove the carbon backing. The sample can be transferred rapidly from one chamber to another and the collision region under UHV conditions.

The aluminium specimens were prepared by evaporating aluminium onto a thin ($\simeq 35$ Å) free standing carbon substrate covering a number of 0.8 mm diameter holes in the target mount. The thickness was monitored by a crystal thickness monitor and judged to be close to 50 Å. The film was sputtered from the carbon side using 800 eV Ar^+ ions, until some of the films broke. Thus, assuming that at this time the carbon film was completely removed, one should have a free-standing polycrystalline aluminium film. Subsequently the film was transferred to the spectrometer and measured. This was all done in three interconnected vacuum chambers as described above without exposing the sample to air. Pressure in the evaporation and sputtering chamber was in the 10^{-9} torr range and in the measurement chamber the pressure was $4 \cdot 10^{-10}$ torr during the experiment. The copper specimens were prepared in a similar way. The Au film was evaporated on NaCl single crystal, floated off in water and transferred on the sample holder. Before the measurement these Au films were further thinned by sputtering as well.

The incident beam can be used as a transmission diffraction facility when the Faraday cup is moved out of the way of the incident beam. This is used to align the target specimen, which is mounted on a manipulator, along a chosen crystal direction. It can also be used to check on the quality of a crystalline sample.

4. Electronic structure theories

4.1 Independent electron model

We employed here the linear-muffin-tin-orbital (LMTO) method [14] which is an efficient and flexible tool for the first-principles computations of elec-

tronic structure of solids. In this method the electronic structure calculation is performed conveniently by dividing the crystal into non-overlapping muffin-tin (MT) spheres centered on atomic sites, and remaining interstitial region. The electron density and the potential are almost spherically symmetric within the MT spheres and are essentially flat in the interstitial region. Therefore the electron wavefunction, the charge density and the potential have a dual representation: spherical harmonic expansion inside the MT spheres and plane wave expansion in the interstitial region.

The LMTO method is just one of many computational schemes derived within the framework of the density functional theory. Great practical advantage of the LMTO method is that only a minimal basis set of energy-independent orbitals (typically 9–16 per atom) is needed to obtain accurate eigenvalues (band energies). In the simplest atomic sphere approximation to the LMTO method the MT spheres are expanded to the overlapping Wigner-Seitz (WS) spheres which occupy the whole volume of the crystal without interstitial region. Inside the WS spheres, the LMTO's are represented by numerical solutions of the radial Schrödinger equation and their energy derivatives. Outside the WS spheres the LMTO's are augmented by the solutions of the Helmholtz's equation at some fixed energy.

We write the one-electron wave function in a crystal in the tight-binding representation as the Bloch sum of the localised MT orbitals:

$$\psi_{j\boldsymbol{k}}(\boldsymbol{r}) = \sum_{\boldsymbol{t}} e^{i\boldsymbol{k}\cdot\boldsymbol{t}} \sum_{\Lambda} a_{\Lambda}^{j\mathbf{k}} \phi_{\Lambda}(\boldsymbol{r} - \boldsymbol{R} - \boldsymbol{t}) \quad . \tag{12}$$

Here $\boldsymbol{k}$ is the crystal momentum, j band index, $\boldsymbol{t}$ translation vector and $\boldsymbol{R}$ basis vector. The label Λ defines a MT orbital centered at a given site $\boldsymbol{R}$ and it comprises the site index $\boldsymbol{R}$ and a set of atomic-like quantum numbers. The expansion coefficients $a_{\Lambda}^{j\mathbf{k}}$ are found by solving the eigenvalue problem using the standard variational technique.

4.2 Electron correlations models

The hole Green's function entering Eq. (6) can be calculated by the many-body perturbation theory (MBPT) expansion on the Bloch waves basis (12). Taking the first non-vanishing term in the MBPT leads to the so-called GW approximation [15, 16]. In this acronym G stands for the Green's function and W denotes the screened Coulomb interaction. The GW approximation is known to give accurate quasiparticle energies [17]. However, its description of satellite structures is not satisfactory. In alkali metals, for example, photoemission spectra show the presence of multiple plasmon satellites whereas the GW approximation yields only one at too large energy. This shortcoming of the GW approximation has been resolved by introducing vertex corrections in the form of the cumulant expansion to the Green's function [18–20]. This allowed the

inclusion of multiple plasmon creation. As a result the calculated peak positions of the plasmon satellites were found in a much better agreement with the experiment than those predicted by the GW scheme itself [21–23].

Formally, the cumulant expansion for the one-hole Green's function can be derived as follows. We choose the time representation for the Green's function, drop the band index j for brevity and write it as

$$G(\boldsymbol{k}, t<0) = i\theta(-t)\, \mathrm{e}^{-i\varepsilon_k t + C^h(k,t)} \tag{13}$$

where ε_k is the one-electron energy and $C^h(\boldsymbol{k}, t)$ is defined to be the cumulant. Expanding the exponential in powers of the cumulant we get

$$G(\boldsymbol{k}, t) = G_0(\boldsymbol{k}, t)\left[1 + C^h(\boldsymbol{k}, t) + \frac{1}{2}[C^h(\boldsymbol{k}, t)]^2 + \ldots\right] \tag{14}$$

where $G_0(\boldsymbol{k}, t) = i\theta(-t)\exp(-i\varepsilon_k t)$. In terms of the self-energy Σ, the Green function for the hole can be expanded as

$$G = G_0 + G_0\Sigma G_0 + G_0\Sigma G_0\Sigma G_0 + \ldots \tag{15}$$

To lowest order in the screened interaction W, the cumulant is obtained by equating

$$G_0 C^h = G_0\Sigma G_0 \tag{16}$$

where $\Sigma = \Sigma_{GW} = iG_0 W$. The first-order cumulant is therefore

$$C^h(\boldsymbol{k}, t) = i\int_t^\infty \mathrm{d}t' \int_{t'}^\infty \mathrm{d}\tau\, \mathrm{e}^{i\varepsilon_k \tau}\Sigma(\boldsymbol{k}, \tau) \tag{17}$$

This is then put back into Eq. (13) yielding multiple plasmon satellites. The energy-momentum representation of the Green's function can be restored by the time Fourier transform.

5. Results

The measured SEMD of occupied states in the conduction band and the $2p$ core level of aluminium is shown in Fig. 2a as a gray-scale intensity plot, darker colour representing higher intensity. Fig. 2b shows the same data after deconvolution of inelastic events using the measured energy loss spectra obtained for the same sample as discussed by Vos *et al.* [24]. The dispersion in the valence band and the associated broad high binding energy contribution due to electron correlation effects is immediately obvious. The core level on the other hand shows no dispersion, but is much broader in momentum-space. Due to momentum-space normalisation, where the high q components

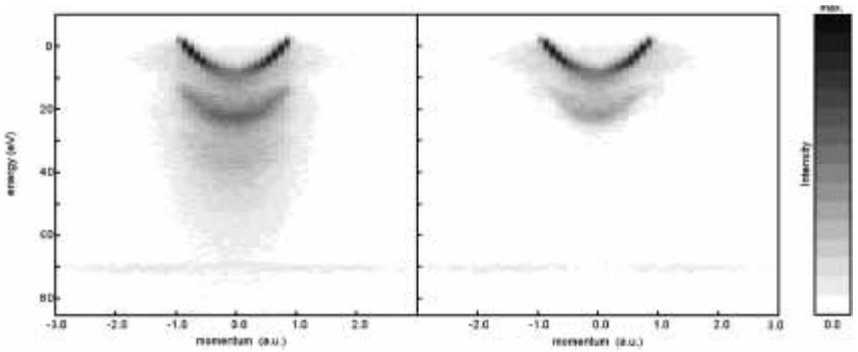

Fig. 2. The measured SEMD for an aluminium target before (left) and after (right) deconvolution of inelastic multiple scattering effects based on measured energy loss spectra. The SEMD includes both the valence band and the $2p$ core band and the density is shown in a linear grey scale.

are weighted by q^2 before integration over q, the density of the $2p$ core level at any q is lower than that of the much more localised (in momentum-space) valence band. Besides the broad tail due to correlations, the other striking feature of the measured uncorrected SEMD in the valence region is that the peak density is not uniform along the band. The peak density at zero momentum (Γ point) is significantly lower than that in the arms of the band. This is due to the band lifetime being much shorter there than nearer to the Fermi level. Thus the width of the band is greater in this region, re-

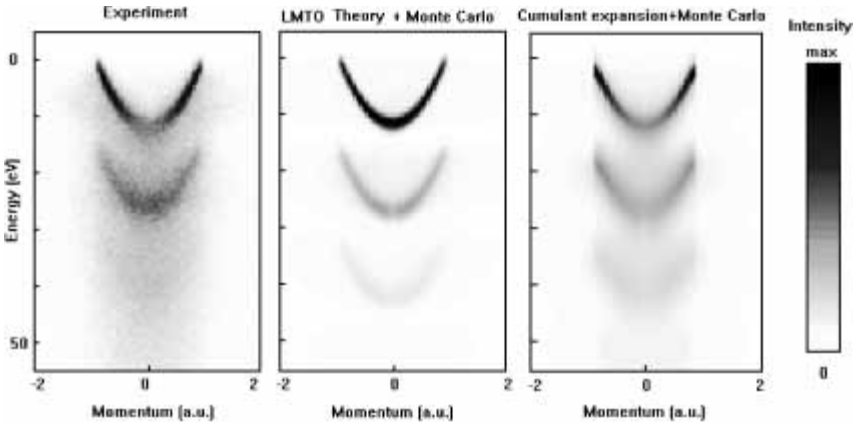

Fig. 3. Energy-momentum densities for aluminium. The left panel shows the measured data, the central panel the calculated density based on Monte Carlo simulations of multiple scattering effects using the LMTO model, whereas the right panel shows the simulation based on the cumulant expansion calculation.

ducing the peak height proportionately, the integral over energy remaining constant.

In Fig. 3 the measured SEMD in the valence region is compared with calculated SEMD's convoluted with multiple scattering effects (both elastic and inelastic) using the Monte Carlo technique. The experimental energy resolution (1.5 eV) and momentum resolution (0.1 a.u.) has also been folded into the calculations. The LMTO theory has no natural width to the band at any q, whereas the many-body cumulant expansion calculation gives a finite lifetime or width to the band as well as density moved to higher binding energies. It reproduces very well the dip in peak density at the Γ point seen in the measurements.

A more detailed comparison between the experimental SEMD and the Monte Carlo simulation of the cumulant expansion calculation is presented in Fig. 4. This shows the momentum profiles at different energies relative to the Fermi level. Due to the finite energy resolution a small amount of density is present above the Fermi level.

Close to the Fermi level there is almost no intensity between the peaks symmetric about $q = 0$. Such background intensity is caused by elastic scattering. The cumulant expansion Monte Carlo simulation describes the data very well at all energies, both in terms of the shapes of the profile and the peak heights.

The measured density for the Al $2p$ core level is compared with a calculated density using the atomic $2p$ Hartree-Fock wave function (dashed line) in Fig. 5. For this localised (in coordinate space) core level the atomic wave function should be a good approximation to that in condensed Al. Indeed the calculated density is very close to the measured one. When the effects of elastic scattering are included (solid line), density is moved from the peak at around 1.5 a.u. to higher and lower momenta filling in the zero minimum at $q = 0$. The simulation is also in very good agreement with the data, although it seems to slightly overestimate the effects of elastic multiple scattering.

The measured SEMD's for copper and gold are shown in Fig. 6 in a gray-scale plot with highest intensity darkest. They are strikingly similar. Hybridisation of the sp-band and the d-band causes a change from the simple parabolic dispersion seen for aluminium. The highest peak density in both cases is near the bottom of the band, in contrast to aluminium. The d-bands are in both cases very extensive in momentum space, quite broad but not dispersive. Due to their large extension in momentum space, their peak intensities at any q are quite small. In copper the sp-band extends to somewhat higher momenta than is the case for gold.

The measured spectral densities for copper are presented in Fig. 7 as binding energy spectra plotted as a function of momentum. They are compared with Monte-Carlo simulations based on LMTO (dashed lines) and many-body cumulant expansion (solid lines) calculations. The LMTO calculation has been folded with energy width of 2.0 eV, to allow for the natural width of the quasi-

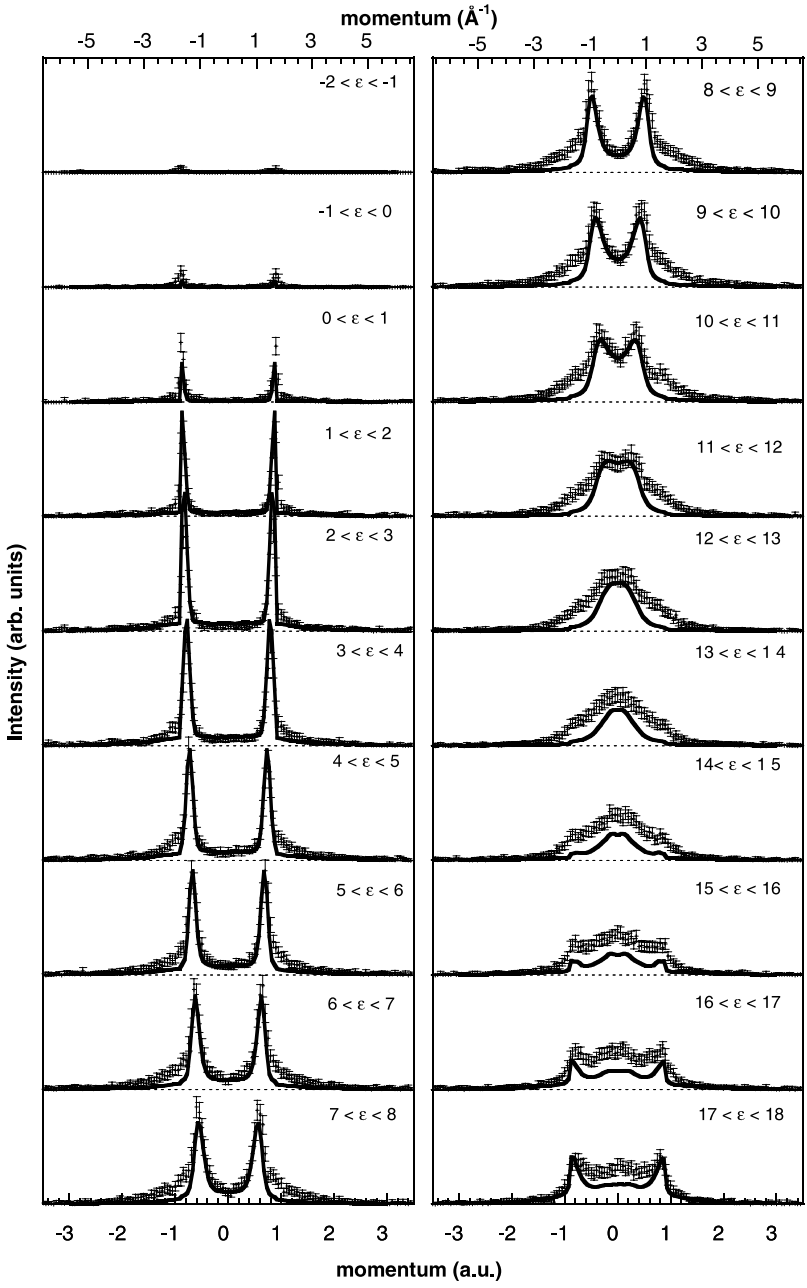

Fig. 4. The momentum profiles at different binding energies ε (relative to the Fermi level) for aluminium. The solid line is the Monte Carlo simulation based on the cumulant expansion many-body calculations of the electronic structure.

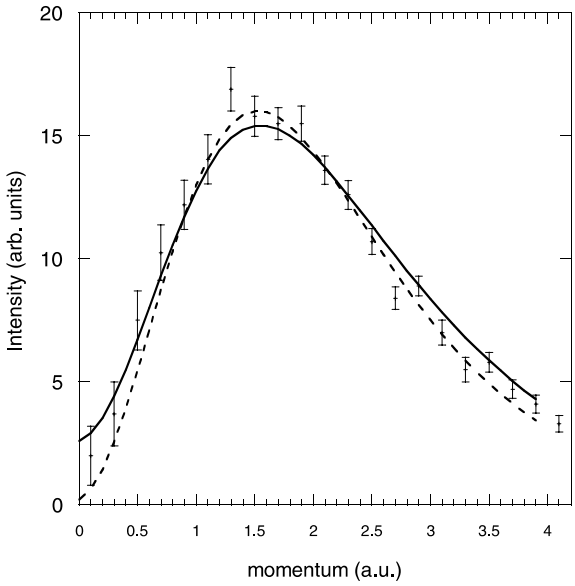

Fig. 5. The measured momentum density for the Al $2p$ core level compared with the Hartree-Fock atomic $2p$ level with (solid line) and without (dashed line) elastic scattering simulations.

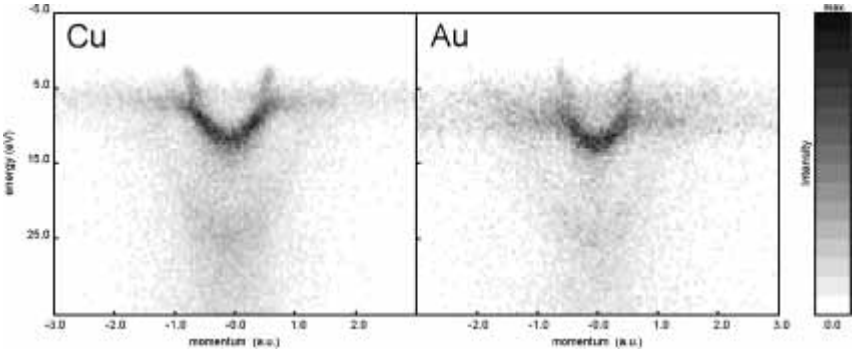

Fig. 6. The measured spectral momentum densities for polycrystalline samples of copper (left panel) and gold (right panel).

particle peak which dominates the binding energy spectra. The many-body calculation predicts the observed quasiparticle peak width very well and explains most of the data. It does not explain the subsidiary peak at around 23 eV for $q < 0.1$ a.u. which disperses to around 18 eV for $0.6 < q < 0.7$ a.u. This peak is very similar both in energy and dispersion to that observed for the σ band in amorphous carbon, and is therefore most probably due to carbon

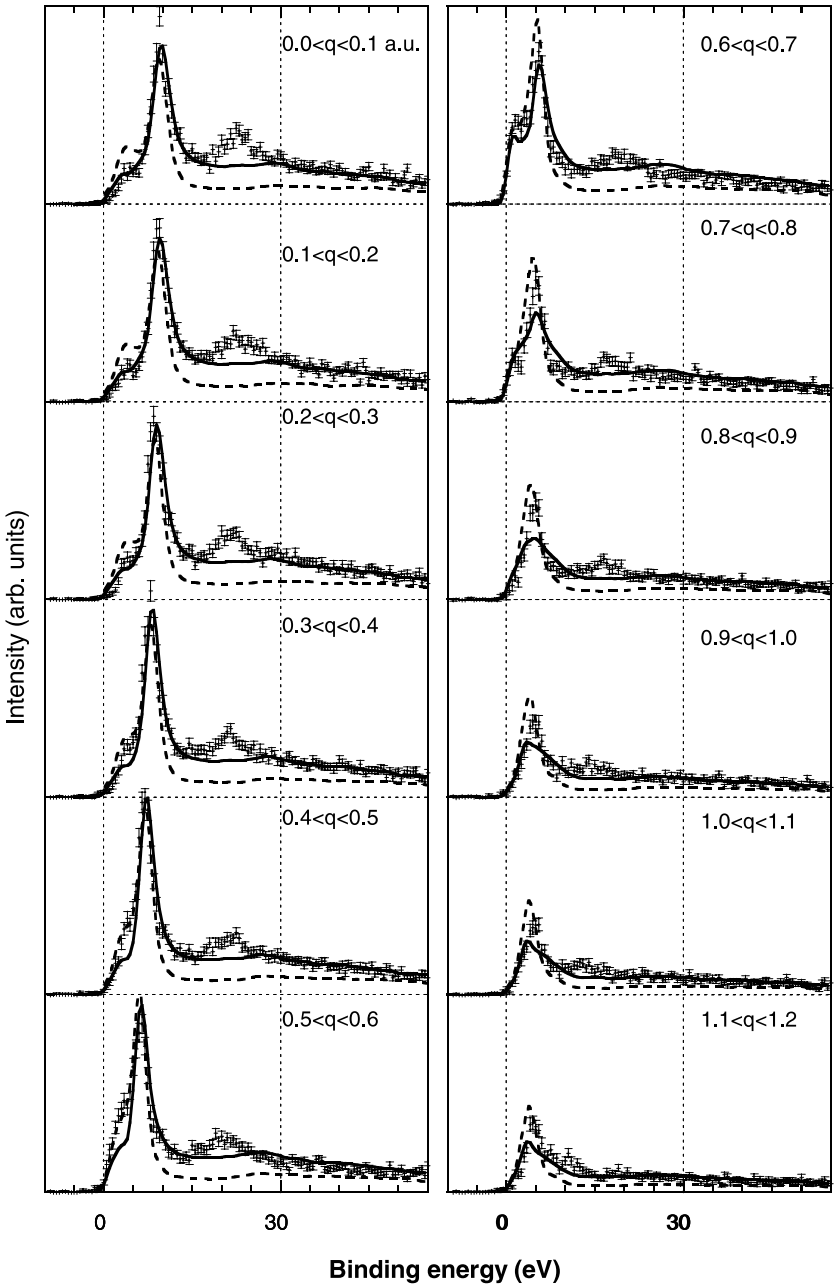

Fig. 7. The measured spectral densities for copper at different momenta compared with Monte Carlo simulations based on the many-body cumulant expansion theory (solid lines) and the LMTO model (dashed lines).

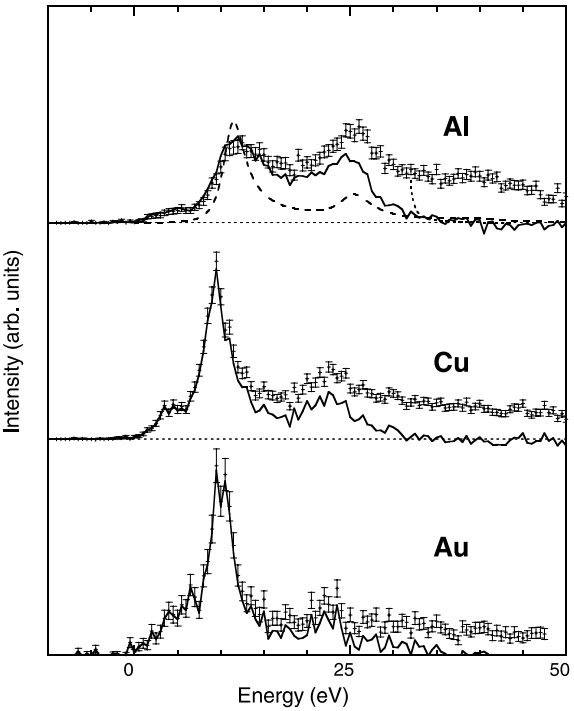

Fig. 8. The measured spectral densities near zero momentum for aluminium, copper and gold deconvoluted for inelastic multiple scattering (solid lines) compared with calculated $\rho\,(q=0,\varepsilon)$ using the cumulant expansion model (long dashes) or the GW approximation (short dashes).

contamination. Traces of carbon could remain on the sample since the film was produced by evaporation onto a thin carbon foil, which was subsequently removed by sputtering.

In Fig. 8 we compare the energy spectra near zero momentum for aluminium, copper and gold with many-body calculations. The raw data are indicated with error bars, whereas the data corrected for inelastic multiple scattering effects are shown by the solid lines. The long dashed lines in the figure are the predicted cumulant expansion spectra through the Γ point ($q=0$) folded with an experimental energy resolution of 2 eV. The short dashed lines are the many-body GW calculation also convoluted with a 2 eV energy resolution.

All the many-body calculations predict a main quasi particle peak of considerable width, but not quite as broad as the measured ones. In the case of aluminium the cumulant expansion calculation predicts a long tail with a subsidiary peak, corresponding to an intrinsic plasmon, at around 25 eV. The position of this peak is in good agreement with the data, but the experiment obtains significantly more density in this region. The experimental peak is at higher en-

ergy than that expected for carbon and therefore it must be primarily due to correlation induced satellite structure in aluminium. The measurements show a very broad quasiparticle peak with about equal strength shifted to higher energies, more than predicted by this calculation. The small intensity below the quasiparticle peak is due to elastic multiple scattering moving intensity from $q \neq 0$ to $q_{\rm obs} = 0$. This can be seen in Fig. 4, where the Monte Carlo simulation, which takes elastic scattering into account, gives non-zero density. A similar effect can be seen in the cases of copper and gold. In the latter case, due to the narrow localisation of the density in momentum space around $q = 0$ and the larger elastic scattering cross section, the effect is somewhat larger. In Fig. 8 the data have been deconvoluted only for inelastic effects, and the effects of elastic multiple scattering have not been included in the theoretical SEMD.

The GW calculation for Al also gives a broad quasi-particle peak at around the measured energy, but the satellite peak is far too narrow and much higher in energy than the observed satellite structure.

In the case of copper the many-body calculations give a broad quasiparticle peak with a long tail. The peak is at slightly higher energy than the observed one and somewhat narrower. As discussed earlier the small peak observed in the data at around 23 eV can most probably be attributed to some carbon contamination resulting from the specimen preparation process. The GW approximation gives a small intrinsic plasmon satellite peak at around 35 eV in disagreement with the data.

For gold both calculations give very similar results and are in very good agreement with the measurements. Again the small peak at around 22–23 eV can most likely be attributed to some carbon contamination of the sample.

6. Conclusions

In this paper we reported EMS measurements, using the new high energy spectrometer at the Australian National University, of the spectral electron momentum densities of the occupied states of polycrystalline metallic samples: aluminium, copper and gold. The SEMD's of copper and gold are quite similar, with the sp-bands hybridising with the essentially non-dispersive d-band. The latter is however very extensive in momentum space.

The data show that all three metals have a broad quasiparticle peak with a short lifetime and satellite structure extending to higher binding energies. The quasiparticle widths are of the order of 4 eV and in the case of aluminium the width at $q = 0$ (the Γ point) is significantly greater than the width at larger q. Thus the peak density for the quasiparticle peak at $q = 0$ is considerably lower than that observed at larger q. For Al the satellite structure due to electron correlations gives rise to a higher energy peak of almost equal density to the "main" quasiparticle peak. The spectral momentum density is very broad in energy at all momenta.

For copper and gold the electron correlations produce a long tail in the quasiparticle peak as well as resulting in its large width and short lifetime.

It is not possible to describe the data using the LMTO approximation. Many-body effects must be included in any theoretical attempt to describe the data. Of the two many-body calculations, the cumulant expansion method provides a much better description of the data compared with the *GW* approximation.

Acknowledgement

It is a pleasure to acknowledge the many fruitful and incisive discussions with Professor Wolf Weyrich on electron momentum densities over many years and to present this article in honour of his sixtieth birthday.

References

1. R. Courths and S. Hüfner, Phys. Rep. **112** (1984) 53.
2. R. N. West, Adv. Phys. **22** (1973) 263.
3. M. Cooper, Rep. Prog. Phys. **48** (1985) 415.
4. P. A. Eisenberger and W. A. Reed, Phys. Rev. A **5** (1973) 2085.
5. P. Schattschneider, *Fundamentals of Inelastic Electron Scattering*, Springer, Berlin (1986).
6. T. Tschentscher, J. R. Schneider and F. Bell, Phys. Rev. B **48** (1993) 16965.
7. T. Sattler, Th. Tschentscher, J. R. Schneider, M. Vos, A. S. Kheifets, D. R. Lun, E. Weigold, G. Dollinger, H. Bross and F. Bell Phys. Rev. B **63** (2001) 155204.
8. I. E. McCarthy and E. Weigold, Phys. Rep. **27C** (1976) 275.
9. E. Weigold and I. E. McCarthy, *Electron Momentum Spectroscopy*, Kluwer Academic/Plenum, New York (1999).
10. M. Vos, G. Cornish and E. Weigold, Rev. Sci. Instrum. **71** (2000) 331.
11. M. Vos and E. Weigold, J. Elec. Spectrosc. & Rel. Phen. **112** (2000) 107.
12. M. Vos and M. Bottema, Phys. Rev. B **54** (1996) 5946.
13. Z. Fang, X. Guo, S. Utteridge, S. A. Conney, I. E. McCarthy, M. Vos, and E. Weigold, Rev. Sci. Instrum. **68** (1997) 4396.
14. H. L. Skriver, *The LMTO Method*, No. 41 in *Springer Series in Solid-State Science*, Springer-Verlag, Berlin (1984).
15. L. Hedin, Phys. Rev. **139** (1965) A796.
16. L. Hedin and S. Lundqvist, Solid State Phys. **23** (1969) 1.
17. F. Aryasetiawan and O. Gunnarsson, Rep. Prog. Phys. **61** (1998) 237.
18. D. Langreth, Phys. Rev. B **1** (1970) 471.
19. B. Bergersen, F. W. Kus, and C. Blomberg, Can. J. Phys. **51** (1973) 102.
20. L. Hedin, Phys. Scr. **21** (1980) 477.
21. F. Aryasetiawan, L. Hedin, and K. Karlsson, Phys. Rev. Let. **77** (1996) 2268.
22. M. Vos, A. Kheifets, E. Weigold, S. Canney, B. Holm, F. Aryasetiawan, and K. Karlsson, J. Phys.: Condensed Matter **11** (1999) 3645.
23. M. Vos, A. S. Kheifets, E. Weigold, and F. Aryasetiawan, Phys. Rev. B **63** (2001) 033108.
24. M. Vos, A. S. Kheifets and E. Weigold, J. Phys. Chem. of Solids, accepted.